Journal of Catalysis 457 (2026) 116828

Contents lists available at ScienceDirect

Journal of Catalysis

journal homepage: www.elsevier.com/locate/jcat

Research article

Forming interfacial Li-Ni-Fe hydride enables room-temperature alkyne semi-hydrogenation

Qiongyu Wang [a], Ziheng Zhang [b], Xilun Zhang [a], Hua Xie [b,*], Ling Jiang [b], Fei Chang [a,*]

[a] Yongjiang Laboratory, Ningbo 315202, China
[b] State Key Laboratory of Chemical Reaction Dynamics, Dalian Institute of Chemical Physics, Chinese Academy of Sciences, Dalian 116023, China

ARTICLE INFO

Keywords:
Alkynes
Hydrogenation
Lithium hydride
Room temperature
Synergy

ABSTRACT

Catalytic alkyne semi-hydrogenation is a pivotal industrial transformation currently constrained by the limitations of existing heterogeneous catalysts: precious metals (e.g., Pd) face high costs, while non-precious alternatives (e.g., Ni, Cu, Fe) generally require harsh reaction conditions (100–200 °C, 10–40 bar H_2). To address these persistent challenges, we propose a novel strategy integrating alkali metal hydrides, serving simultaneously as hydrogen donors and anionic "ligands" into transition metal systems. Herein, we report a NiFe-LiH composite catalyst that enables efficient and highly selective liquid-phase semi-hydrogenation of alkynes—including aliphatic, aromatic, and heteroatom-substituted substrates under very mild conditions (25 °C, ≤3 bar H_2). Mechanistic investigations reveal that reactive hydride species (H^-) are integral to the hydrogenation catalysis. Critically, the formation of unique Li-Ni-Fe-H interfacial species facilitate synergistic interactions wherein anionic hydrides coordinate with transition metals, modulating their electronic states to simultaneously enhance catalytic activity and selectivity. This work demonstrates room-temperature activation and transformation of alkynes enabled by a catalytic Li-Ni-Fe-H system, offering a promising new pathway for developing efficient non-noble metal catalysts for selective hydrogenation reactions.

1. Introduction

Catalytic hydrogenation is a fundamental step in chemical synthesis. The selective semi-hydrogenation of alkynes (C≡C) to alkenes (C=C) represents not only a critical industrial process but also a prototypical model reaction of great scientific interests [1]. This transformation enables the green production of high-value compounds such as pharmaceutical intermediates, fragrances, and agricultural commodities, while serving as an essential purification method for olefin feedstocks in the petrochemical operations [2,3]. Therefore, catalyst development for this reaction system continues to attract considerable research attention. Conventional alkyne semi-hydrogenation processes employ Lindlar catalysts ($Pd/Pb(OAc)_2$ on $CaCO_3$) [4]. However, these catalysts suffer from inherent toxicity and low atomic utilization efficiency, which has driven the development of numerous alternatives. Despite significant advances in the hydrogenation catalyst design over recent decades, persistent challenges include dependence on precious metals and limited substrate scope [5,6]. Consequently, designing efficient and environmentally friendly non-noble metal catalysts for selective C≡C bond reduction remains both a significant goal and an ongoing challenge.

The high cost and scarcity of precious metals have stimulated significant research in non-precious metal catalysts in recent years. Among these, Ni-based catalysts, particularly Raney Ni, have gained widespread industrial adoption for hydrogenation reactions due to their relatively high hydrogenation activity [7,8]. However, in alkyne selective hydrogenation, conventional Ni catalysts exhibit excessive activity toward both hydrogenolysis and polymerization of carbon–carbon bonds, leading to low selectivity and poor stability [9–11]. Recent advances have focused on designing single-atom or alloy catalysts to optimize the adsorption configuration of reaction intermediates, modulate reaction energy barriers and steer hydrogenation pathways [12–14]. One prominent strategy involves incorporating a second metal. For instance, Clarysse et al. developed Zn-rich Ni_3Zn nanocrystals, in which zinc doping isolates Ni active sites and weakens C=C adsorption, achieving excellent semi-hydrogenation selectivity [2]. Similar "active site isolation" effects have been demonstrated by using secondary metals, including Ga [15], Au [16], and Sn [17]. Alternatively, modifying Ni dispersion through composite supports has proven effective: Ni supported on high-surface-area mesoporous silica leverages ordered channels to achieve high dispersion and selectivity [5]. Nevertheless, non-

* Corresponding authors.
E-mail addresses: xiehua@dicp.ac.cn (H. Xie), fei-chang@ylab.ac.cn (F. Chang).

https://doi.org/10.1016/j.jcat.2026.116828
Received 24 January 2026; Received in revised form 10 March 2026; Accepted 11 March 2026
Available online 17 March 2026

precious metal catalysts typically require tough reaction conditions (100–200 °C, 10–40 bar). Yet, as a compromise, such systems often suffer from significantly diminished activity at lower temperatures.

Another critical factor governing hydrogenation efficiency is the adsorption and activation of molecular hydrogen (H_2) [18]. Metal hydrides, characterized by high redox potential and hydrogen transfer reactivity, offer distinct advantages in chemical transformations due to their unique functionalities, particularly for hydrogen-involved catalytic reactions at mild conditions [19–21]. For instance, Chen's group has reported applications of metal hydrides in ammonia synthesis [22], hydrogenolysis of aniline to arenes [23], and deuterated compound synthesis via hydrogen isotope exchange [24]. Similarly, Chang et al. demonstrated that carbon-supported KH catalysts efficiently catalyze toluene hydrogenolysis to benzene [25]. Hydride species also serve as key intermediates in alkyne hydrogenation reactions [26]. For example, de Jongh et al. reported that lattice hydride (H^-) in $NaAlH_4$ can be extracted directly and utilized in alkyne hydrogenation [27]. Chang et al. further demonstrated a transition-metal-free catalyst KH/MgO capable of activating dihydrogen and selectively semi-hydrogenating diphenylacetylene to stilbene under certain conditions (<80 °C and < 20 bar H_2) [3].

Building on this foundation, here we propose a strategy for developing new non-noble metal catalysts for alkyne hydrogenation: integrating alkali metal hydrides, serving as both a hydrogen donor and an anionic "ligand", into transition metal catalyst systems. The coordination of hydride with the metal alloys preserves the uniform nature of the active sites, while the presence of H^- maintains high hydrogenation activity. This approach may effectively enhance hydrogenation performance without sacrificing activity or selectivity at low temperatures. Herein, we report an NiFe-LiH composite catalyst that achieves selective hydrogenation of diverse alkyne substrates, including aliphatic alkynes, aromatic alkynes, and heteroatom-containing alkynes, under exceptionally mild conditions (25 °C, ≤ 3 bar H_2). Using 4-ethynyltoluene as a model substrate, we optimized reaction conditions to achieve high conversion (> 99%) and high selectivity to 4-vinyltoluene (95%). Mechanistic studies reveal that the hydrogenation process is significantly influenced by the regulation of NiFe electronic states and the presence of reactive hydride species, both resulting from the formation of the Li-Ni-Fe-H interface.

2. Results and discussion

Transition metal-lithium hydride composites (Ni-LiH, Fe-LiH, and NiFe-LiH) were synthesized via a solid-state ball-milling method (Fig. 1a). Inductively coupled plasma optical emission spectroscopy (ICP-OES) analyses (Table S1) confirmed that the actual contents of Ni, Fe, and Li align closely with theoretical values. The NiFe-LiH materials with varying Fe doping levels are denoted as $NiFe_n$-LiH, where n represents the Fe/Ni molar ratio. X-ray diffraction (XRD) patterns (Fig. 1b) of the composites exhibit diffraction peaks at 44.4° and 51.6°, corresponding to the (1 1 1) and (2 0 0) planes of metallic Ni, respectively, while peaks at 38.1° and 64.5° are attributed to LiH. Notably, no

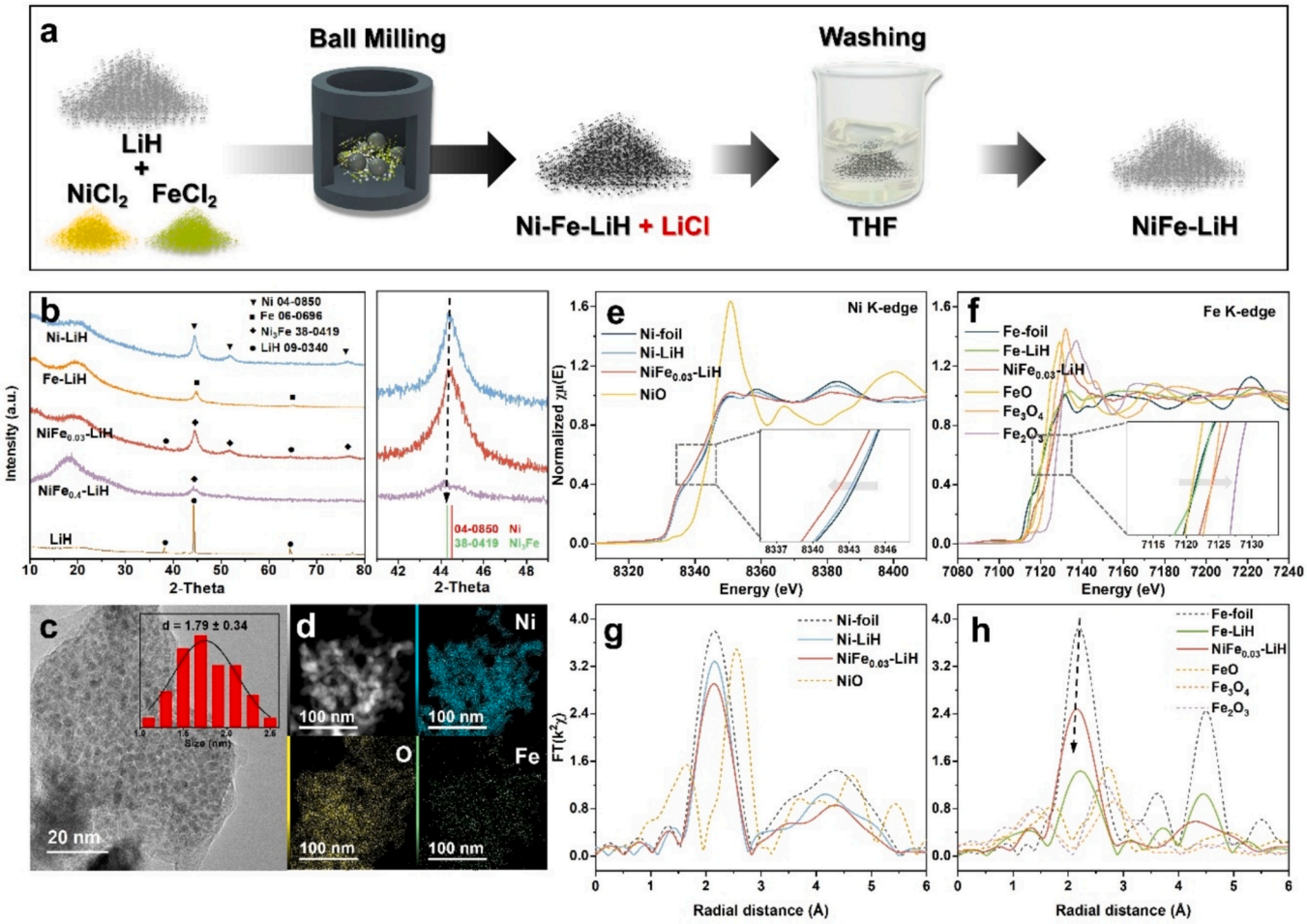

Fig. 1. (a) Schematic illustration for the preparation procedure of NiFe-LiH. (b) XRD patterns of LiH, Ni-LiH, Fe-LiH, $NiFe_{0.03}$-LiH and $NiFe_{0.4}$-LiH. (c) High resolution TEM images and particle size distribution diagram of $NiFe_{0.03}$-LiH. (d) HAADF-STEM image, and corresponding EDX elemental maps of $NiFe_{0.03}$-LiH. (e) Ni K-edge and (f) Fe K-edge XANES of the $NiFe_{0.03}$-LiH catalysts and references. (g) Ni K-edge and (h) Fe K-edge EXAFS spectra of the $NiFe_{0.03}$-LiH and references.

characteristic peaks of metallic Fe were observed in $NiFe_{0.03}$-LiH due to its low loading. As Fe doping increased, the Ni diffraction peak shifted to lower angles (from 44.4° in Ni-LiH to 44.2° in $NiFe_{0.4}$-LiH), indicating the formation of an Fe-Ni alloy phase [28,29]. High resolution transmission electron microscope (HR-TEM) images reveal tiny NiFe nanocrystals dispersed on LiH (Fig. 1c), with an average particle size of 1.8 nm (Fig. 1d). Lattice fringes assignable to Fe species were absent when comparing the HR-TEM images and analyzing lattice fringes of Ni-LiH and NiFe-LiH (Figs. S1 and S2), likely owing to the negligible mass contrast between Fe and Ni atoms. Nevertheless, high-angle annular dark field-scanning transmission electron microscopy (HAADF-STEM) imaging and energy-dispersive X-ray spectroscopy (EDX) elemental mapping (Figs. 1d and S3) confirmed the homogeneous dispersion of Fe across the catalyst surface.

The chemical states and local coordination environments of Ni and Fe in the composites were further elucidated via X-ray absorption fine structure (XAFS) spectroscopy. As shown in the K-edge XANES spectra (Fig. 1e and f), Ni exhibits metallic states and Fe is positively charged. Notably, the pre-edge features of $NiFe_{0.03}$-LiH differ significantly from those of monometallic Ni-LiH and Fe-LiH [28]. Specifically, the Ni absorption edge in $NiFe_{0.03}$-LiH shows a negative shift relative to that in Ni foil and Ni-LiH, suggesting an electron-rich state of Ni compared to Ni^0 [30]. Conversely, the Fe K-edge absorption shifts to higher energies relative to Fe foil and Fe-LiH, and lies between those of FeO and Fe_2O_3. These results demonstrate that Fe doping modulates the electron density around Ni species, consistent with electron transfer from Fe to Ni. Furthermore, the Fe K-space oscillation peaks shift toward lower k-values (Fig. S4), implying increased disorder around Fe sites [31]. To probe the coordination structures, Fourier transforms of the EXAFS spectra in R-space were analyzed. $NiFe_{0.03}$-LiH displays a prominent peak at ~2.15 Å (Fig. 1g), matching the conventional Ni-Ni bond distance (~2.16 Å). In contrast, the first-shell peak of Fe contracts markedly from 2.19 Å (Fe-Fe bond distance in Fe foil) to 2.14 Å (Fig. 1h), indicating shortened bond lengths attributable to Ni-Fe coordination [32–34]. This observation aligns with the k-space oscillation features. Fe-O or Ni-O peak is absent in $NiFe_{0.03}$-LiH.

Using 4-ethynyltoluene (4-ET) as a model substrate, the selective hydrogenation performance of different catalysts was evaluated at 25 °C under 3 bar H_2 (Fig. 2a). LiH and Fe-LiH show negligible catalytic activity with only 0.1% and 0.7% conversion after 6 h (Table S2), whereas Ni-LiH achieve 38% conversion. Remarkably, NiFe-LiH attains >99% conversion under identical conditions with 95% selectivity toward the target semi-hydrogenation product 4-vinyltoluene (4-VT). Both ball-milled and commercial NiFe nano-powders exhibit negligible catalytic activity in the absence of hydride. Replacing LiH with Li_2O or LiOH drastically reduces catalytic activity, confirming the indispensable role of LiH in catalyzing alkyne hydrogenation at room temperature. Notably, NiFe-LiH substantially outperforms the physical mixture of Ni-LiH and Fe-LiH, highlighting the critical importance of the solid-state ball-milling synthesis strategy. This performance enhancement is primarily attributed to the formation of NiFe-LiH interface. The 4-ET conversion rate exhibits a volcano-type dependence on the Fe/Ni molar ratio (Fig. S5), with optimal activity at 0.01–0.03. Besides, we also evaluated the influence of NiFe to LiH weight ratios on the

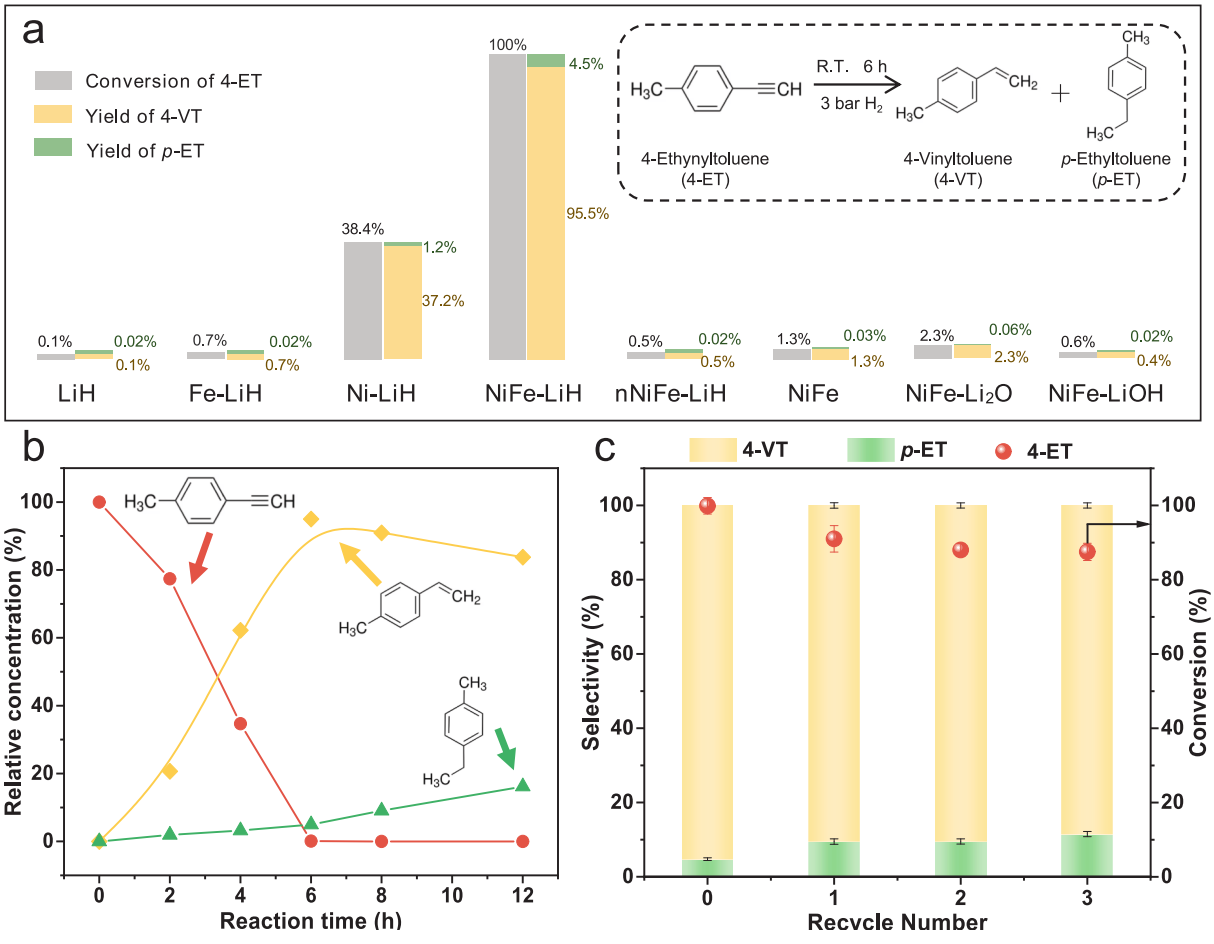

Fig. 2. (a) Selective hydrogenation of 4-Ethynyltoluene (4-ET) on different catalysts at 25 °C and 3 bar H_2 for 6 h. (b) Change of relative concentrations of 4-ET and its hydrogenation products as a function of reaction time on the $NiFe_{0.03}$-LiH catalyst. (c) Recycle tests of catalytic hydrogenation of 4-ET on $NiFe_{0.03}$-LiH. Reaction conditions: 25 °C, 3 bar H_2, 6 h, 30 mg of catalyst, a 10:1 M ratio of 4-ET to transition metal, 5 ml of toluene was used as solvent. Error bars represent the standard deviation of independent experiments.

hydrogenation activity. Notably, the 64 wt%NiFe-36%wt % LiH sample remains optimal (Fig. S6), suggesting the ratio of NiFe to LiH is critical and may be explained by the necessity to form interfacial Li-Ni-Fe hydride, which will be discussed later. The activity decline at higher iron loadings correlates with nanoparticle aggregation (as evidenced by HAADF-STEM images, particle size distribution diagram and corresponding EDX elemental mappings of $NiFe_{0.4}$-LiH in Fig. S7) and consequent active-site coverage.

Fig. 2b illustrates the temporal evolution of 4-ET and its hydrogenation products over the $NiFe_{0.03}$-LiH catalyst. Complete conversion of 4-ET is achieved within 6 h, with 4-VT as the primary product (95% selectivity). Upon prolonged reaction, over-hydrogenation became evident: 4-VT selectivity decreases to 84% at 12 h, accompanied by the gradual accumulation of the over-hydrogenation product *p*-ethyltoluene (*p*-ET). This time-dependent product distribution indicates kinetically controlled hydrogenation on $NiFe_{0.03}$-LiH. The hydrogen pressure dependence (Fig. S8) further demonstrates that 3 bar H_2 suffices for complete 4-ET conversion while maintaining 95% 4-VT selectivity, highlighting the catalyst's superior semi-hydrogenation ability even at room temperature. Elevated pressures significantly reduce 4-VT selectivity.

The reusability of the $NiFe_{0.03}$-LiH catalyst was evaluated through consecutive reaction cycles (Fig. 2c). Only a marginal activity decrease is observed after three cycles, due to inevitable catalyst loss during materials separation and recovery. Notably, the 4-VT selectivity remains stable throughout all cycles. Post-reaction characterization of the recovered catalyst (Figs. S9–S10) reveals unchanged crystal structures in XRD patterns and TEM images. Furthermore, catalytic performance under high substrate concentration was assessed. At a substrate to transition metal molar ratio of 50:1, complete 4-ET conversion is achieved within 7 h at 25 °C under 6 bar H_2. Crucially, this fivefold increase in substrate loading requires no significant intensification of reaction conditions, underscoring the exceptional efficiency of the catalytic process. Additionally, ICP-OES analysis of the supernatant from the mixture of $NiFe_{0.03}$-LiH catalyst and reactant solution treated under stirring at 3 bar H_2 reveals no detectable Ni, Fe, or Li (Table S3). This collected supernatant also does not present any activity for the hydrogenation of 4-ET. These results indicate that no catalytic active species leached into the reaction solvent, thus confirming the heterogeneous nature of the catalytic process in this study.

To assess the broad scope of the $NiFe_{0.03}$-LiH catalyst for alkyne semi-hydrogenation reactions, its performance toward diverse substrates was evaluated at ambient temperature in 1–3 bar H_2 (Fig. 3 and Table S4). Hydrogenation of phenylacetylene affords styrene with 89% selectivity at 74% conversion, while diphenylacetylene hydrogenation achieves 86% conversion and 80% selectivity toward *cis*-stilbene, versus only 2% for *trans*-stilbene. The catalyst also exhibits excellent activity towards alkyl-substituted alkynes, for instance 1-phenyl-1-propyne (Entry 3), and 1-butyl-4-ethynylbenzene (Entry 4). In the case of 1-phenyl-1-propyne, hydrogenation catalysis yields the *cis*-hydrogenated product with remarkable 91% selectivity. Furthermore, the catalyst achieves highly efficient and selective hydrogenation of aliphatic alkynes: hydrogenation of 1-octyne (Entry 5) yields 1-octene with 76% selectivity in 97% conversion. For a longer-chain substrate, 1-decyne (Entry 6) achieves complete conversion (100%), yielding 1-decene with 91% selectivity. Notably, the $NiFe_{0.03}$-LiH catalyst demonstrates outstanding selectivity and exceptional functional group tolerance in the semi-hydrogenation of heteroatom-substituted phenylacetylene derivatives. Substrates with halogen (F, Cl, Br; Entries 7, 8, 9), aldehyde (Entry 10), cyano (Entry 11), methoxy (Entry 12), and amino (Entry 13) groups consistently achieve high conversion and semi-hydrogenation selectivity as shown in Fig. 3 and Table S4. The observed variations in performance across substrates may arise from differences in their steric and electronic effects.

To elucidate the active sites and hydrogenation pathways, we conducted a series of control experiments. Notably, in the absence of H_2, the hydrogenation of 4-ET over $NiFe_{0.03}$-LiH at 25 °C under 1 bar Ar atmosphere yields 23% conversion of 4-ET and 95% selectivity to 4-VT (Fig. S11). This observed activity clearly indicates the participation of hydride species originating from LiH in the hydrogenation catalysis. Subsequently, LiH, Ni-LiH, Fe-LiH, and NiFe were tested under identical conditions, respectively. No hydrogenation activity is observed for NiFe,

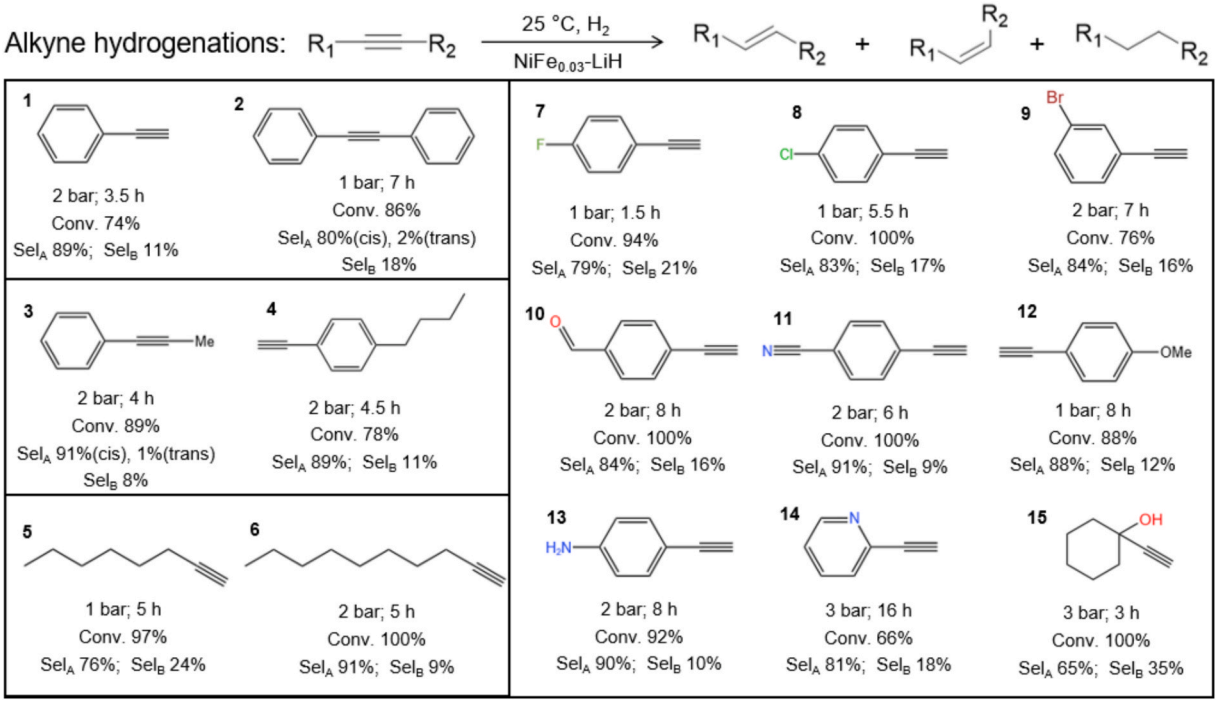

Fig. 3. Substrate scope study of alkyne hydrogenations on $NiFe_{0.03}$-LiH. Sel_A: selectivity to alkene; Sel_B: selectivity to alkane. All reactions were performed at 25 °C. H_2 pressure applied and reaction time were noted below each of the substrate. Catalyst loadings were: 10 mol% for substrates 1, 5–8, 13; 6.6 mol% for substrate 3; 5 mol% for substrates 2, 4, 9–12, 14–15. Solvents used were: toluene for substrates 1, 3–4, 7–10, 12–15; mesitylene for substrates 2, 5–6; acetone for substrate 11.

LiH, or Fe-LiH. In contrast, Ni-LiH exhibits a 12% conversion of 4-ET. This activity trend ($NiFe_{0.03}$-LiH > Ni-LiH > NiFe/Fe-LiH/LiH ≈ 0) is consistent with their respective catalytic performances shown in Fig. 2.

Next, we employed temperature-programmed desorption-mass spectrometry (TPD-MS) to investigate the hydrogen release behavior of the composite catalyst (Fig. 4a). Pure LiH exhibits significant H_2 desorption only at temperatures >400 °C due to its thermal stability. Minor H_2 release from FeNi powder is detected between 200 and 400 °C, attributed to chemisorbed dihydrogen on FeNi surfaces during material preparation. Notably, $NiFe_{0.03}$-LiH shows a H_2 desorption upon heating, indicating strong interaction between NiFe and LiH that facilitates lithium-transition metal hydride species formation [35]. Under these inert conditions, the observed H_2 desorption profiles reflect the intrinsic thermal stability of the materials or the synergistic interaction between NiFe and LiH in the composite, free from kinetic interference by surface reaction. However, it is crucial to emphasize that this hydride activation is not limited to thermal pathways: upon exposure to alkyne at room temperature, NiFe-LiH readily releases H_2 and generates hydride vacancies, a key step enabling alkyne hydrogenation. As shown in Fig. S12, an intense H_2 desorption peak emerges immediately upon switching the gas feed from Ar to C_2H_2 at 25 °C, confirming rapid room-temperature hydride-alkyne coupling. More importantly, hydrogen desorption suggests hydride vacancy generation on the catalyst surface. These vacancies are essential for subsequent dihydrogen activation and hydrogenation catalysis. The TPD results align with earlier hydrogen-free catalytic activity tests (Fig. S11), supporting a mechanism where LiH acts as a hydrogen donor, followed by vacancy formation and in situ hydride regeneration via gaseous H_2 replenishment [3,24,27].

Gas-phase mass spectroscopy was conducted on the $NiFe_{0.03}$-LiH composite catalyst to probe the formation of lithium-transition metal hydride. As shown in Fig. 4b, the most intense peak observed at m/z = 167 amu for clusters generated from the NiFe-LiH catalyst is assigned to $[LiNiFe(LiH_2)_5]^-$. Previous studies indicated strong metal-hydrogen interaction at multivalent hydride interfaces [35,36]. The anionic $[LiH_2]^-$ provides highly reactive H^- species, consistent with both TPD results and the electron-rich state features observed in the Ni K-edge XANES spectrum. Collectively, these findings elucidate the active sites at the NiFe/LiH interface, explaining the origin of superior catalytic activity on $NiFe_{0.03}$-LiH. The mass spectrum also shows multiple polyhydride clusters such as $[LiNi_3H(LiH_2)_n]^-$ (n = 0, 2, 4, 6), previously observed in Ni-LiH (Fig. S13). Given the significant activity difference between NiFe-LiH and Ni-LiH, we propose that Fe incorporation and the synergistic FeNi/LiH interaction forming the Li-Ni-Fe hydride interface are essential for enhanced hydrogenation activity.

To elucidate the hydrogenation pathway of 4-ET over the $NiFe_{0.03}$-LiH catalyst, we employed in-situ diffuse reflectance infrared Fourier transform spectroscopy (DRIFTS) to monitor spectral evolution in real time under reaction conditions. Following the introduction of 4-ET onto the catalyst surface and subsequent Ar purging, distinct spectral features emerge (Fig. 4c): two discrete bands at 3300 cm^{-1} and 2100 cm^{-1} are assigned to the ≡C–H stretching vibration and the C≡C asymmetric stretching vibration of adsorbed 4-ET, respectively. Upon exposure to a H_2 flow at room temperature, progressive attenuation of both the ≡C–H and C≡C signals occur, confirming the initiation of hydrogenation

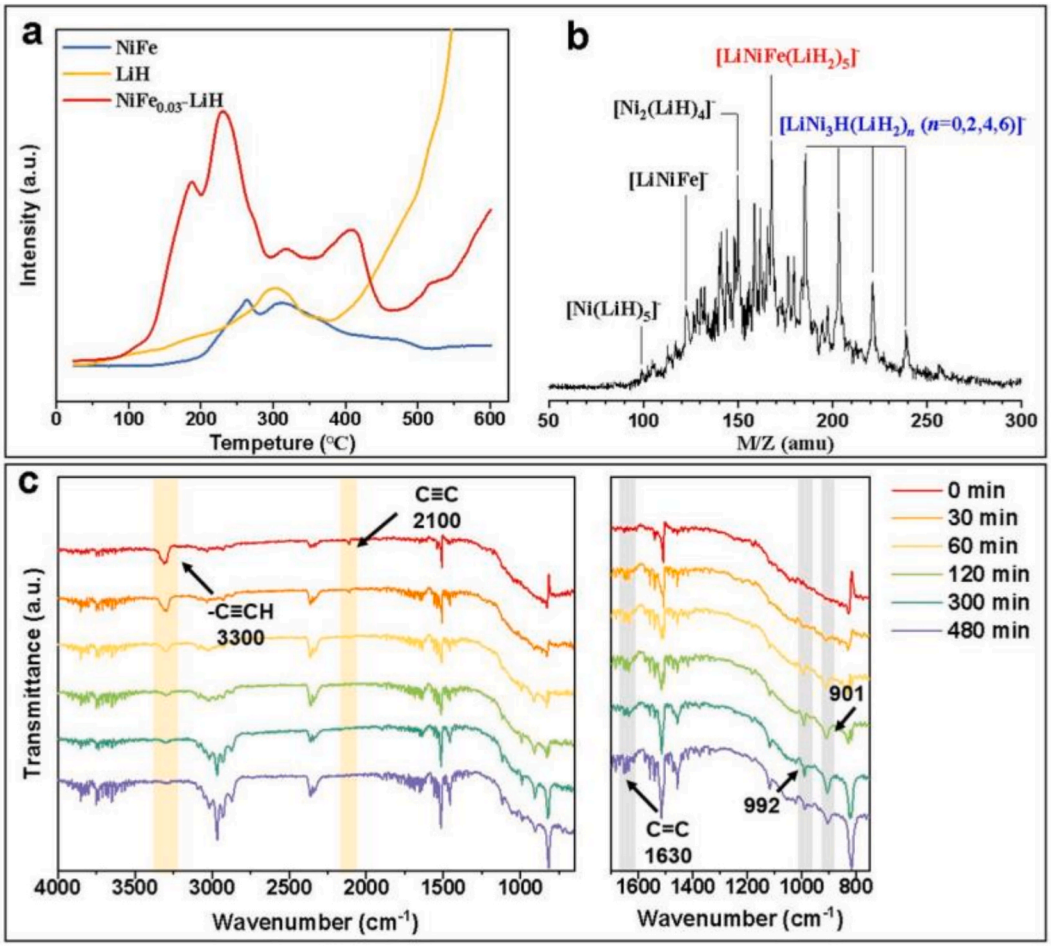

Fig. 4. (a) Ar-TPD of $NiFe_{0.03}$-LiH with H_2 signal (m/z = 2) monitored by a mass spectrometer. (b) Mass spectrum of the species produced by pulsed laser vaporization of the $NiFe_{0.03}$-LiH target in the presence of a helium carrier gas. (c) Monitoring the catalytic hydrogenation process of 4-ET on $NiFe_{0.03}$-LiH using in situ DRIFTS. Reaction was conducted at 25 °C under 1 bar H_2.

catalysis. Concurrently, enhanced intensity in the 3100–2900 cm^{-1} region (attributed to aromatic C–H vibrations) suggests strong catalyst-aromatic ring interactions [37,38], potentially involving reported alkali metal cation-π interactions [3,31]. As the C≡C signal diminishes, three new peaks rapidly emerge at 1630 cm^{-1}, 992 cm^{-1}, and 901 cm^{-1}, assigned to the C=C stretching vibration, the out-of-plane and in-plane C–H bending vibrations of the C=C–H group in vinyl species, respectively [39,40]. These characteristic peaks provide direct spectroscopic evidence for the formation of the target semi-hydrogenation product 4-VT. The rapid accumulation of 4-VT, reaching maximum concentration near complete 4-ET conversion, again demonstrates the high activity and selectivity of $NiFe_{0.03}$-LiH for alkyne semi-hydrogenation. Subsequent spectral evolution reveals decreased =C–H signal intensity alongside the emergence of a new band at 2970–2850 cm^{-1}, characteristic of aliphatic C–H stretching vibrations [41]. This shift indicates the onset of 4-VT over-hydrogenation, yielding the saturated alkane, *p*-ET. Crucially, over-hydrogenation is only observed after near-complete consumption of 4-ET, suggesting a kinetically controlled hydrogenation mechanism.

Finally, we investigated dihydrogen activation on NiFe-LiH and the incorporation of hydride during hydrogenation catalysis. H_2-D_2 exchange experiment was performed in a flow reactor at 25 °C and 1 bar pressure. A flow of D_2 or H_2 was fed to the sample alternately and the transient gas products were probed by an on-line mass spectrometer. As shown in Fig. S14, once D_2 was introduced to the reactor, formation of HD was immediately observed. At this point the signal of HD grows sharply, after which it decreases in a short period of time due to the complete exchange of activated hydrogen in NiFe-LiH by deuterium. This itinerary production of HD by alternate feeding of D_2 or H_2 evidences that LiH acts as a hydrogen donor at room temperature. Then, hydrogen tracking experiments were performed (Fig. S15). Using GC–MS isotopic labeling: (1) With NiFe-LiD + C_9H_8 (in Ar) → $C_9H_8D_2$ + $C_9H_8D_4$, proving hydride (D^-) delivery from LiD to the reactant; (2) With NiFe-LiH + C_9H_8 (in D_2) → $C_9H_7D_3$ + $C_9H_8D_4$, proving D^- incorporation via D_2 activation after vacancy formation. These experiments demonstrate that NiFe-LiH can interact with alkyne by H_2 elimination to form hydride vacancy at room temperature, and once the hydride vacancy forms, H_2 can dissociate and replenish the vacancy. The hydride transfer mechanism is plausible, i.e., incorporation of hydride in NiFe-LiH catalyst directly participate into the hydrogenation reaction. These combined H_2-D_2 exchange and isotopic hydride-tracking experiments provide direct experimental evidence for a dynamic hydride-mediated catalytic cycle in NiFe-LiH. Specifically, at room temperature, the catalyst undergoes reversible H_2 elimination from surface hydride sites, generating transient hydride vacancies on the Li-Ni-Fe-H. Critically, these vacancies serve as highly active sites for subsequent H_2 dissociation sustaining catalyst integrity over multiple turnover cycles. The incorporated hydride (H^-) is directly transferred to the adsorbed alkyne substrate likely via σ-bond metathesis, forming a vinylic intermediate that proceeds to full hydrogenation. This hydride transfer mechanism reconciles the observed high activity under mild conditions. Regarding to the influence of Fe incorporation, as evidenced by our XAS data, electron transfer from Fe to Ni occurs in the NiFe-LiH catalyst. Gas-phase mass spectrometry identified the surface species $[LiNiFe(LiH_2)_5]^-$, a hydrogen-rich Li-Ni-Fe-H interfacial motif. We propose that Fe incorporation exerts a dual role: (1) electronically modulating Ni (via charge transfer), and (2) templating a geometrically distinct, cooperative Li-Ni-Fe-H interface that enhances alkyne adsorption and facilitates concerted hydride transfer during hydrogenation. While the precise local coordination and dynamic structure of this motif remain unresolved in the present work, its spectroscopic detection will be a key direction for future work.

3. Conclusion

In summary, we report a transition metal-alkali metal hydride composite catalyst (NiFe-LiH) fabricated via solid-state synthesis. The optimized NiFe-LiH catalyst enables efficient and selective hydrogenation of diverse alkynes-including aliphatic, aromatic, and heteroatom-containing substrates at room temperature and 1–3 bar H_2. The hydrogenation reaction over $NiFe_{0.03}$-LiH is kinetically controlled, with selectivity toward target alkenes tunable by adjusting reaction time and pressure. Under optimized conditions (25 °C, 3 bar H_2), the model substrate 4-ethynyltoluene achieves near 100% conversion with 95% selectivity to 4-vinyltoluene. The formation of unique Li-Ni-Fe-H interfacial species facilitate synergistic interactions: the anionic hydride coordinates with the transition metals, modulating their electronic states to simultaneously enhance catalytic activity and selectivity, offering a promising pathway to break the traditional performance limitations in alkyne semi-hydrogenation.

4. Methods section

4.1. Chemicals

All chemicals were of analytical grade, purchased from the indicated vendors, and used without any further purification: nickel chloride (anhydrous, 98%, Alfa), ferrous chloride (anhydrous, ≥99.5%, Aladdin), lithium hydride (≥97%, Aladdin), lithium hydroxide (≥99%, Aladdin), lithium oxide (99%, Aladdin), tetrahydrofuran (99.9%, Innochem), iron powder (≥99.9% metals basis, Aladdin), nickel powder (≥99.9% metals basis, Aladdin), toluene (99.5%, Sinopharm), mesitylene (98%, Innochem), acetone (≥99.5%, Sinopharm). Substrates used include: 4-ethynyl toluene (98%, Aladdin), phenylacetylene (≥97%, Aladdin), 4-fluorophenylacetylene (98%, Aladdin), 1-chloro-4-ethynylbenzene (≥98%, Aladdin), 3-bromophenylacetylene (≥97%, Aladdin), 4-acetylbenzenamine (≥98%, Aladdin), 1-phenyl-1-propyne (>98%, Aladdin), 4-acetylbenzaldehyde (≥97%, Aladdin),4-methoxyphenylacetylene (99%, Aladdin), 1-butyl-4-ethynylbenzene (≥96%, Aladdin), 4-ethynylbenzonitrile (≥97%, Aladdin), 2-ethynylthiophen (≥97%, Aladdin), 1-octyne (95%, Aladdin), 1-decyne (≥97%, Aladdin), diphenylacetylene (99%, Aladdin), 4-methyl-4-ethoxy diphenylacetylene (≥99%, Aladdin), 1-acetyl-1-cyclohexanol (99%, Macklin). All chemicals were stored in an argon-filled glove box. Gases were supplied directly from high-pressure cylinders without further purification: hydrogen (99.999%, Linde Gas) and argon (99.999%, Linde Gas).

4.2. Catalysts preparation

TMs-LiH composites catalysts (Ni-LiH, Fe-LiH, and $NiFe_x$-LiH) were synthesized via a mechanochemical reaction between the corresponding TM chlorides ($NiCl_2$ and/or $FeCl_2$) and LiH. Typical preparation procedure is as below (take Ni-LiH as an example): $NiCl_2$ (500 mg) and LiH (215 mg) were mixed in a molar ratio of LiH:$NiCl_2$ = 7:1. The solid mixture was mechanically activated using a planetary ball-milling machine operated at 200 revolutions per minute (rpm) for 3 h. A solid-state reaction occurred during the ball-milling process: $2LiH + FeCl_2 = Fe + 2LiCl$. The black solid product was purified by washing three times with anhydrous tetrahydrofuran (THF) to remove LiCl, the byproduct. The final product was isolated after vacuum drying. Because LiH was added in an excess amount, composition of the final product is metallic Ni and LiH. The recovered mass of the Fe-LiH composite is 95% of the theoretical yield, which indicates minimal loss of material during synthesis. Based on stoichiometric calculations (accounting for LiCl removal), the final molar ratio of Fe to LiH in the composite was 1:5. The same procedures were employed to synthesize Fe-LiH, and $NiFe_n$-LiH (the subscript *n* represents the molar ratio of Fe to Ni in the composite). ICP-OES was performed to determine the actual loadings of Ni, Fe, and Li. Results were shown in Table S1, which were consistent with the theoretical stoichiometries of these composites.

Preparation of NiFe powder: $NiCl_2$ (490 mg), $FeCl_2$ (10 mg) and LiH (62 mg) were mixed, ball-milled and purified (to remove LiCl by-

product) as the same procedure used above.

NiFe-Li_2O and NiFe-LiOH were prepared following the same ball-milling method. NiFe powder (200 mg), prepared via the aforementioned method, were mixed with Li_2O (508 mg) or LiOH (407 mg) as the starting materials, respectively.

4.3. Materials characterization

X-ray diffraction (XRD) patterns were recorded using CuKα radiation (wavelength 1.5418 Å) on a Bruker AXS D8 Advance XRD instrument. Hermetically sealed sample holders were used to prevent air intrusion. Inductively coupled plasma-optical emission spectrometer (ICP-OES, Perkin Elmer avio560) was used to determine the content of Ni, Fe, and Li in the catalysts. Scanning transmission electron microscopy combined with energy-dispersive X-ray spectroscopy (STEM-EDX) was performed using a JEOL JEM-F200 system featuring a high-brightness field-emission gun (FEG), complemented by a high-angle annular dark-field (HAADF) detector and a wide-collection-angle EDX detector. Fourier transform infrared (FTIR) spectra were collected using a Nicolet TM iS50 FTIR Spectrometer via DRIFT mode. Samples were prepared in an argon-filled glovebox then transferred to air-tight sealed cells. Extended X-ray Absorption Fine Structure (EXAFS) measurements were performed using a benchtop Rapid-XAFS spectrometer (Anhui Absorption Spectroscopy Instruments Co., Ltd.). Sample was sealed with Kapton film to prevent air contamination. Programmed temperature decomposition (TPD) experiments were conducted in a fixed-bed reactor. The exhaust gas analyzed by a Hiden mass spectrometer and employed to investigate the hydrogen release behavior of the NiFe-LiH composite catalyst due to the interaction between NiFe and LiH. All samples were brought out from the glovebox and transfer for TPD experiments without exposing to air, moisture or any pretreatment. In a typical measurement, 50 mg of sample was used, and heat up to the desired temperature with a ramp rate of 5 °C min^{-1} in an argon flow of 30 ml min^{-1}.

4.4. General procedure for the catalytic hydrogenation reactions

In an Ar-filled glovebox, 30 mg of catalysts, 286–453 mg of the corresponding alkyne substrate (a substrate to transition metal molar ratio ranging from 10 to 20) and 5–10 mL of solvents (toluene, mesitylene or acetone) were added into an autoclave equipped with a glass liner. The autoclave was sealed, brought out from the glovebox, and connected to a high-pressure line of Ar or H_2. All low-pressure experiments were conducted in a custom-built gas-handling system equipped with a high-accuracy digital pressure transducer (validity certified to ±0.01 bar, calibrated against NIST-traceable dead-weight standard). Prior to each run, the system underwent leak testing and zero/full-scale calibration using pure Ar or H_2 gas was performed per month. The line was purged (3 times with H_2) and the autoclave pressurized to a set pressure of Ar or H_2 and heated to the desired temperature (ramping rate was 5 °C min^{-1}). The stirring rate was 600 rpm. Except for the recycling experiments, after the test the reaction mixture was open in air, filtered (filter paper), and the supernatant collected and analyzed by GC–MS (after adding a known amount of internal standard). For the recycling experiments, after a test the autoclave was transferred into the Ar-filled glovebox. The liquid part of the reaction mixture was collected for the GC–MS analysis, and a new batch of solvent (5 mL) was added for the subsequent test. The obtained solution is quantitatively analysed by gas chromatography (GC, Agilent 8890 GC) with a HP-5 or Innowax column. Typical GC profiles for all measurements were presented in Figs. S16 and S17.

Conversion and selectivity were calculated according to the following equations:

$$\text{Conversion (alkyne)} = \frac{[\text{alkyne}]_0 - [\text{alkyne}]}{[\text{alkyne}]_0} \times 100\%$$

$$\text{Selectivity (alkene)} = \frac{[\text{alkene}]}{[\text{alkyne}] + [\text{alkene}] + [\text{alkane}]}$$

$$\text{Yield (alkene)} = \text{Conversion (substrate)} \times \text{Selectivity (alkene)} \times 100\%$$

where $[\text{alkyne}]_0$ and [alkyne] are the concentrations (mmol/L) of alkyne substrate before and after the reaction, respectively.

4.5. Gas-phase mass spectroscopy

Gas-phase mass spectroscopy was carried out using a home-made instrument with a laser vaporization source and a dual-channel time-of-flight (D-TOFMS) mass spectrometer. Details of the apparatus have been described elsewhere [1], and only a brief outline of the experiment is given below. The species were generated via the pulsed laser vaporization cluster source using the second harmonic of a Nd:YAG laser. The catalyst was ablated in the presence of a supersonic beam of carrier gas, and the typical stagnation pressure of carrier gas was about 2–6 bar. Under the efficient cooling by supersonic expansion of pulsed helium carrier gas, the clusters were cooled to ~200 K in the vacuum chamber. The cluster ions were analyzed by the TOF mass spectrometer.

CRediT authorship contribution statement

Qiongyu Wang: Writing – original draft, Investigation. **Ziheng Zhang:** Investigation. **Xilun Zhang:** Investigation. **Hua Xie:** Writing – review & editing, Supervision, Funding acquisition. **Ling Jiang:** Writing – review & editing, Supervision, Funding acquisition. **Fei Chang:** Writing – review & editing, Supervision, Methodology, Funding acquisition, Conceptualization.

Declaration of competing interest

The authors declare that they have no known competing financial interests or personal relationships that could have appeared to influence the work reported in this paper.

Acknowledgment

This research was supported by Zhejiang Provincial Natural Science Foundation of China under Grant No. LR24B030002, and the National Natural Science Foundation of China (Grant Nos. 22273101, 22125303, and 92361302). The authors acknowledge the Material Analysis and Testing Center (YongV) of Yongjiang Laboratory for providing access to equipment used in the materials characterization experiments conducted in this study.

Appendix A. Supplementary data

Supplementary data to this article can be found online at https://doi.org/10.1016/j.jcat.2026.116828.

Data availability

Data will be made available on request.

References

[1] X. Deng, J. Wang, N. Guan, L. Li, Catalysts and mechanisms for the selective heterogeneous hydrogenation of carbon-carbon triple bonds, Cell Rep. Phys. Sci. 3 (9) (2022) 101017.
[2] J. Clarysse, J.D.J. Silva, Y. Xing, S.B.X.Y. Zhang, S.R. Docherty, N. Yazdani, M. Yarema, C. Copéret, V. Wood, Earth-abundant Ni-Zn nanocrystals for efficient alkyne semihydrogenation catalysis, Nat. Commun. 16 (1) (2025) 4378.
[3] X. Zhang, H. Liang, F. Chang, Magnesium oxide-supported potassium hydride as a transition-metal-free catalyst for the selective hydrogenation of alkynes, J. Catal. 440 (2024) 115851.

[4] H. Lindlar, Ein neuer Katalysator für selektive Hydrierungen, Helv. Chim. Acta 35 (2) (1952) 446–450.
[5] Y. Hu, M. Liu, S. Bartling, H. Lund, H. Atia, P.J. Dyson, M. Beller, R.V. Jagadeesh, A general and robust Ni-based nanocatalyst for selective hydrogenation reactions at low temperature and pressure, Sci. Adv. 9 (48) (2023) eadj8225.
[6] D. Wang, D. Astruc, The golden age of transfer hydrogenation, Chem. Rev. 115 (13) (2015) 6621–6686.
[7] Murray Raney. Method for Producing Finely Divided Nickel, US Pat., 1628190, 1927.
[8] Z. Sun, Z.-H. Zhang, T.-Q. Yuan, X. Ren, Z. Rong, Raney Ni as a versatile catalyst for biomass conversion, ACS Catal. 11 (16) (2021) 10508–10536.
[9] J. Su, Y. Ji, S. Geng, L. Li, D. Liu, H. Yu, B. Song, Y. Li, C. Pao, Z. Hu, X. Huang, J. Lu, Q. Shao, Core–shell design of metastable phase catalyst enables highly-performance selective hydrogenation, Adv. Mater. 36 (7) (2024) 2308839.
[10] J. Wang, M. Wang, X. Li, X. Gu, P. Kong, R. Wang, X. Ke, G. Yu, Z. Zheng, Bidentate ligand modification strategy on supported ni nanoparticles for photocatalytic selective hydrogenation of alkynes, Appl. Catal. B-Environ. 313 (2022) 121449.
[11] C. Sui, H. Ma, F. Huang, M. Wang, X. Cai, J. Diao, P. Ren, X. Wen, L. Jin, G. Wang, D. Ma, H. Liu, Fully exposed nickel clusters for semihydrogenation of acetylene, ACS Catal. 14 (19) (2024) 14689–14695.
[12] Z. Wang, Q. Luo, S. Mao, C. Wang, J. Xiong, Z. Chen, Y. Wang, Fundamental aspects of alkyne semi-hydrogenation over heterogeneous catalysts, Nano Res. 15 (12) (2022) 10044–10062.
[13] X. Ge, M. Dou, Y. Cao, X. Liu, Q. Yuwen, J. Zhang, G. Qian, X. Gong, X. Zhou, L. Chen, W. Yuan, X. Duan, Mechanism driven design of trimer ni1sb2 site delivering superior hydrogenation selectivity to ethylene, Nat. Commun. 13 (1) (2022) 5534.
[14] K. Liu, R. Qin, N. Zheng, Insights into the interfacial effects in heterogeneous metal nanocatalysts toward selective hydrogenation, J. Am. Chem. Soc. 143 (12) (2021) 4483–4499.
[15] D.L. Trimm, I.O.Y. Liu, N.W. Cant, The selective hydrogenation of acetylene over a Ni/SiO_2 catalyst in the presence and absence of carbon monoxide, Appl. Catal. A-Gen. 374 (1–2) (2010) 58–64.
[16] B. Yang, R. Burch, C. Hardacre, G. Headdock, P. Hu, Origin of the increase of activity and selectivity of nickel doped by Au, Ag, and Cu for acetylene hydrogenation, ACS Catal. 2 (6) (2012) 1027–1032.
[17] L. Huang, F. Tang, F. Hao, H. Zhao, W. Liu, Y. Lv, P. Liu, W. Xiong, H. Luo, Tuning the electron density of metal nickel via interfacial electron transfer in Ni/MCM-41 for efficient and selective catalytic hydrogenation of halogenated nitroarenes, ACS Sustain. Chem. Eng. 10 (9) (2022) 2947–2959.
[18] L. Zhang, M. Zhou, A. Wang, T. Zhang, Selective hydrogenation over supported metal catalysts: from nanoparticles to single atoms, Chem. Rev. 120 (2) (2020) 683–733.
[19] S. Gnaim, A. Bauer, H.-J. Zhang, L. Chen, C. Gannett, C.A. Malapit, D.E. Hill, D. Vogt, T. Tang, R.A. Daley, W. Hao, R. Zeng, M. Quertenmont, W.D. Beck, E. Kandahari, J.C. Vantourout, P.-G. Echeverria, H.D. Abruna, D.G. Blackmond, S. D. Minteer, S.E. Reisman, M.S. Sigman, P.S. Baran, Cobalt-electrocatalytic HAT for functionalization of unsaturated C–C bonds, Nature 605 (7911) (2022) 687–695.
[20] H. Wan, X. Yang, S. Zhou, L. Ran, Y. Lu, Y. Chen, J. Wang, F. Pan, Enhancing hydrogen storage properties of MgH2 using FeCoNiCrMn high entropy alloy catalysts, J. Mater. Sci. Technol. 149 (2023) 88–98.
[21] H. Yu, X. Li, J. Zheng, Beyond hydrogen storage: metal hydrides for catalysis, ACS Catal. 14 (5) (2024) 3139–3157.
[22] J. Guo, P. Chen, Interplay of alkali, transition metals, nitrogen, and hydrogen in ammonia synthesis and decomposition reactions, Acc. Chem. Res. 54 (10) (2021) 2434–2444.
[23] Y. Cai, W. Liu, Y. Yu, L. Liu, Q. Pei, H. Wu, T. He, J. Guo, A. Wu, P. Chen, Transition metal-free hydrogenolysis of anilines to arenes mediated by lithium hydride, J. Am. Chem. Soc. 144 (38) (2022) 17441–17448.
[24] Y. Cai, L. Rao, Y. Wang, F. Chang, T. He, Y. Zhao, J. Yu, H. Wen, J. Hao, A. Wu, B.-T. Guan, J. Guo, P. Chen, Fabrication of atomically dispersed barium hydride catalysts for the synthesis of deuterated alkylarenes, Nat. Commun. 16 (1) (2025) 1868.
[25] F. Chang, A. Fedorov, Production of benzene by the hydrodemethylation of toluene with carbon-supported potassium hydride, ChemSusChem 16 (2) (2023) e202202029.
[26] T. Wan Kim, D. Kim, S. Hyun Kim, Y. Suh, Heterolytic H2 activation in heterogeneous hydrogenation/hydroprocessing catalysis, ChemCatChem 16 (8) (2024) e202301581.
[27] P.L. Bramwell, J. Gao, B. De Waal, K.P. De Jong, R.J.M. Klein Gebbink, P.E. De Jongh, A transition-metal-free hydrogenation catalyst: pore-confined sodium alanate for the hydrogenation of alkynes and alkenes, J. Catal. 344 (2016) 129–135.
[28] J. Zhao, X. Guo, R. Shi, G.I.N. Waterhouse, X. Zhang, Q. Dai, T. Zhang, NiFe nanoalloys derived from layered double hydroxides for photothermal synergistic reforming of CH4 with CO_2, Adv. Funct. Mater. 32 (31) (2022) 2204056.
[29] G. Shi, T. Tano, D.A. Tryk, A. Iiyama, M. Uchida, K. Terao, H. Osada, M. Yamaguchi, K. Tamoto, K. Kakinuma, Nanostructured Pt-NiFe oxide catalyst for hydrogen evolution reaction in alkaline electrolyte membrane water electrolyzers, ACS Catal. 14 (12) (2024) 9460–9468.
[30] C. Li, W. Zhang, Y. Cao, J. Ji, Z. Li, X. Han, H. Gu, P. Braunstein, J. Lang, Interfacial electronic interactions between ultrathin NiFe-MOF nanosheets and Ir nanoparticles heterojunctions leading to efficient overall water splitting, Adv. Sci. 11 (28) (2024) 2401780.
[31] M. Zhang, C. Xu, Q. Gao, T. Li, K. Zhang, S. Wang, X. Yin, H.-Q. Peng, J. Cheng, Z. Li, B. Liu, Second coordination sphere-regulated nickel sites enable enhanced photocatalytic eight-electron reduction of carbon dioxide to methane, ACS Catal. (2025) 14611–14626.
[32] Y. Shao, C. Wu, S. Xi, P. Tan, X. Wu, S. Saqline, W. Liu, Halite-structured (MgCoNiMnFe)O high entropy oxide (HEO) for chemical looping dry reforming of methane, Appl. Catal. B-Environ. 355 (2024) 124191.
[33] H. Yuan, M. Hong, X. Huang, W. Qiu, F. Dong, Y. Zhou, Y. Chen, J. Gao, S. Yang, Graphene chainmail shelled dilute Ni–Cu alloy for selective and robust aqueous phase catalytic hydrogenation, Adv. Sci. 11 (13) (2024) 2304349.
[34] W. Ren, X. Tan, W. Yang, C. Jia, S. Xu, K. Wang, S.C. Smith, C. Zhao, Isolated diatomic Ni-Fe metal–nitrogen sites for synergistic electroreduction of CO_2, Angew. Chem. Int. Ed. 58 (21) (2019) 6972–6976.
[35] P. Wang, H. Xie, J. Guo, Z. Zhao, X. Kong, W. Gao, F. Chang, T. He, G. Wu, M. Chen, L. Jiang, P. Chen, The formation of surface lithium–iron ternary hydride and its function on catalytic ammonia synthesis at low temperatures, Angew. Chem. Int. Ed. 129 (30) (2017) 8842–8846.
[36] N. Klopčič, I. Grimmer, F. Winkler, M. Sartory, A. Trattner, A review on metal hydride materials for hydrogen storage, J. Energy Storage 72 (2023) 108456.
[37] C.-X. Wang, S. Wang, L.-H. Song, B. Wang, G.-Z. Chen, D.-W. Gao, G.-X. Zheng, Y.-P. Lv, Atomic-level confinement of PtCu nanoclusters within MFI-Type zeolite enables unprecedented kinetics in alkyne semi-hydrogenation, Rare Met. (2025).
[38] Z. Wang, H. Wang, Y. Shi, C. Liu, L. Wu, CuPd alloy decorated SnNb2O6 nanosheets as a multifunctional photocatalyst for semihydrogenation of phenylacetylene under visible light, Chem. Eng. J. 429 (2022) 132018.
[39] D.L. Pavia, G.M. Lampman, G.S. Kriz, J.A. Vyvyan, Introduction to Spectroscopy, Cengage Learning, 2008.
[40] W. Liu, C. Otero Arean, S. Bordiga, E. Groppo, A. Zecchina, Selective phenylacetylene hydrogenation on a polymer-supported palladium catalyst monitored by FTIR spectroscopy, ChemCatChem 3 (1) (2011) 222–226.
[41] Y. Hu, L. Sun, Z. Sun, J. Zhao, A new story for aryl alkynes removal in excess alkenes by supported AuPd, Chem. Eng. J. 505 (2025) 159196.